Optics Letters

A silicon source of frequency-bin entangled photons

Federico Andrea Sabattoli,[1,†] Linda Gianini,[2,*] Angelica Simbula,[2,‡] Marco Clementi,[1,·] Antonio Fincato,[3] Frederic Boeuf,[4] Marco Liscidini,[1] Matteo Galli,[1] and Daniele Bajoni[2]

[1]Dipartimento di Fisica, Università di Pavia, 27100 Pavia, Italy
[2]Dipartimento di Ingegneria Industriale e dell'Informazione, Università di Pavia, 27100 Pavia, Italy
[3]STMicroelectronics, 20010 Cornaredo, Italy
[4]STMicroelectronics, 38920 Crolles, France
*Corresponding author: linda.gianini01@universitadipavia.it
‡Now at: Photonic Systems Laboratory (PHOSL), Swiss Federal Institute of Technology Lausanne (EPFL), CH-1015 Lausanne, Switzerland

Received 22 July 2022; revised 21 October 2022; accepted 1 November 2022; posted 1 November 2022; published 00 xxxxxx 0000

We demonstrate an integrated source of frequency-entangled photon pairs on a silicon photonics chip. The emitter has a coincidence-to-accidental ratio exceeding 10^3. We prove entanglement by showing two-photon frequency interference with a visibility of 94.6% ± 1.1%. This result opens the possibility of on-chip integration of frequency-bin sources with modulators and the other active and passive devices available in the silicon photonics platform.

https://doi.org/10.1364/OL.471241

The generation of entangled states of light in integrated photonics devices is of paramount importance for a number of quantum technologies [1], including several protocols in quantum communication, quantum simulation, and computing. In general, entanglement between two photons can be produced using different degrees of freedom. Polarization-based entanglement [2] constitutes the most widespread choice for free space experiments and applications, while path-based [3] entanglement is the most obvious choice for on chip quantum information processing.

When considering fiber propagation of photonic qubits for quantum communication protocols using optical networks, neither polarization nor path entanglement are viable choices, as phase noise due to thermal fluctuations in fibers would quickly destroy the quantum coherence of the qubits thus encoded. A possible choice for fiber propagation has been, up to very recently, time-bin entanglement [4]. However, time-based entanglement protocols rely on the use of interferometers with a large unbalance between their arms in the receiving units [5], and the need for active stabilization of such interferometers makes a widespread adoption of quantum communication protocols in fiber networks of difficult practical implementation.

Frequency qubits have been shown in recent years to be an interesting alternative to all previous encodings. In the frequency-bin encoding, the two levels used for the qubit state are two optical modes of well-defined and well-separated frequencies [6–9]. In particular, frequency-bin encoding is resistant to amplitude fluctuations in fiber networks and the analysis of the qubit state relies on the use of optical modulators, which can be an alternative to the use of phase-stabilized interferometers [10,11]. Several realizations of integrated devices capable of emitting frequency-bin optical qubits through spontaneous four-wave mixing (SFWM) have been reported in the last decade, where the qubits were encoded using pairs of resonances chosen within the emission comb of a high quality factor (high-Q) silicon nitride [12] or silicon oxynitride [10,13] ring resonator. However, this scheme presents a trade-off between efficiency and bin separation limiting the choice of the ring radius. On the one hand, the frequency separation, given by the ring's free spectral range (FSR), should be a few 10s of gigahertz to operate efficiently with commercially available modulators, thus forcing us to keep the radius large enough. On the other hand, the generation rate of photon pairs in ring resonators is inversely proportional to the square of the ring radius [14], and therefore the emission rate was limited in such demonstrations. Silicon nitride and silicon oxynitride allow one to fabricate resonators with very high-Q, which guarantee high generation rates even with small FSRs. However, these materials are amorphous, and the generation of photon pairs is polluted by a strong Raman photoluminescence [15].

In this work, we present the generation of frequency-bin entangled photons in a silicon photonic integrated circuit employing a design firstly proposed in Ref. [16]. This approach allows us to directly engineer the frequency spacing between the bins independently of the radii of the generating rings. We show internal generation rates R as high as 5×10^5 Hz and a violation of the CHSH inequality [17] by 22 standard deviations without the need to subtract accidental counts, a necessary condition in most quantum information protocols.

The sample layout is shown in Fig. 1. A Mach–Zehnder interferometer is used to pump the two ring resonators independently in an add-drop configuration, with the two rings coupled to the same output waveguide. A continuous wave (CW) laser is used as a pump, and the difference between the distances of each ring from the interferometer's outputs (~ 1 mm) is much shorter than the pump's coherence length (~ 200 m). The two rings are designed with slightly different radii, so that their FSRs differ by ~ 2 GHz.

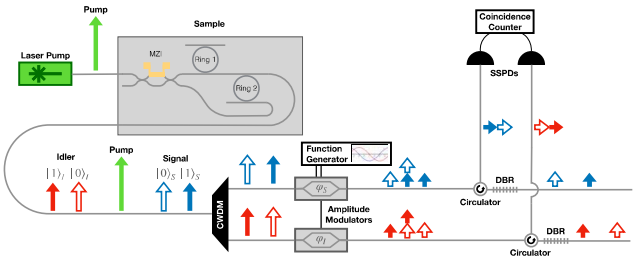

Fig. 1. Scheme of the sample and of the experimental apparatus. The dark rectangle represents the integrated device, connected to an external fiber array with input and output grating couplers, not shown in the picture.

The device was realized in a 310 nm-thick silicon layer on a 300 mm silicon-on-insulator wafer, patterned with 193 nm immersion lithography to partially etch it down to 160 nm [18]. The 400 nm-wide rib waveguide propagation losses are estimated to be 1.7 dB/cm at 1550 nm, with effective index $n_e = 2.79$ and group index $n_g = 3.89$. To get the FSR difference of 2 GHz in the C-band, the radii of the rings were set to 40.8 μm and 41.1 μm.

A transmission spectrum from the sample is shown in Fig. 2(a). The spectrum was taken by routing all the laser intensity to the upper output of the integrated Mach–Zehnder interferometer, so that the through ports of both ring resonators are observed. Several resonances are visible, superimposed to the large bell profile given by the grating couplers. The heaters on top of the two rings are operated so that their resonances at 1551.3 nm ($\nu_p = 193.25$ THz) are perfectly aligned, so that they can later be used to pump both ring resonators simultaneously. For each ring, we label the pump resonance mode #0, and attribute increasing numbers to modes at higher frequency and decreasing numbers to modes at lower frequencies. The radius mismatch results in an increasing frequency displacement $\Delta\nu$ between the resonances of the two rings when increasing the mode number in both directions, so that the sample essentially acts as a Vernier scale in frequency. The frequency displacement between the modes of the two ring resonators is plotted as a function of the mode # in Fig. 3 along with the average

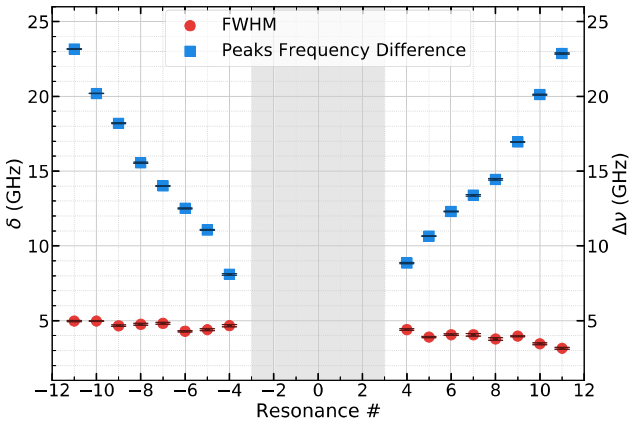

Fig. 3. Average linewidth δ (left-hand axis, red circles) and frequency displacement $\Delta\nu$ (right-hand axis, blue squares) between the modes of the two ring resonators as a function of the resonance number [resonance #0 is the one used for the pump, see Fig. 2(c)]. We report only the range of data in which the two resonances are distinguishable.

linewidth δ for the two rings. The separation is found to increase by ~ 2 GHz per # as designed, while δ always remains below 5 GHz (measured Qs were between 30,000 and 50,000). As clearly visible in the figure, by choosing resonances at a sufficient distance from the pump one can obtain frequency bins with spacing much larger than the linewidth.

We chose resonances separated by eight FSRs from the pump to act as signal and idler resonances. The measured transmission from the modes is reported in Figs. 2(b)–2(d). The signal and idler resonances have $\Delta\nu \sim 15$ GHz, well-above their linewidth but still compatible with commercial optical modulators. We indicate with $|0\rangle$ the frequency-bin states associated with photons emitted by the larger ring, and with $|1\rangle$ the states associated with photons emitted by the smaller ring. The Mach–Zehnder interferometer is operated so that two rings have equal probability of emitting a photon pair, while maintaining the emission rates low enough that the probability of double pair emission remains negligible. Under these conditions the two-photon pair in the output waveguide is the maximally entangled

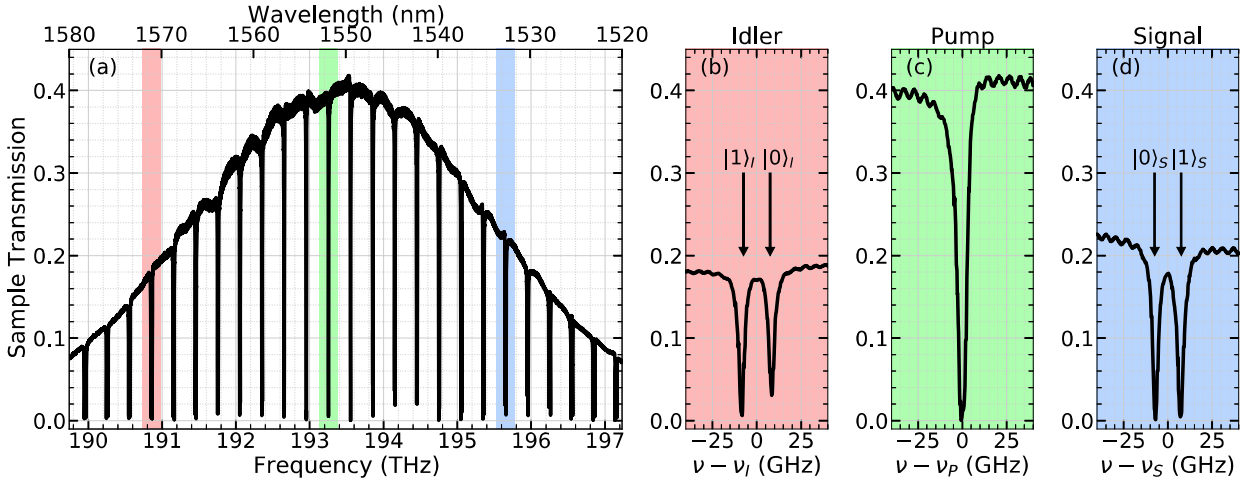

Fig. 2. (a) Transmission spectrum for the sample and larger-scale spectra of the resonances used for (a) the signal photons, (b) the pump, and (c) the idler photons. In panels (b), (c), and (d) the horizontal axes refer to frequencies relative to the idler frequency (ν_I), the pump frequency (ν_P), and the signal frequency (ν_S), respectively.

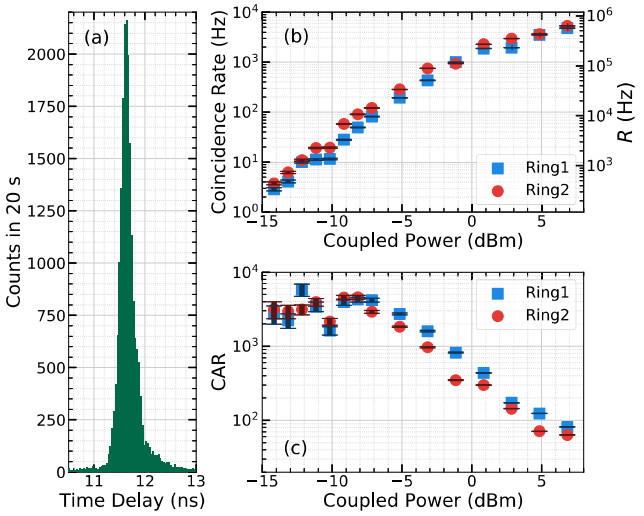

Fig. 4. Four wave mixing experiments. (a) An example of coincidence curve from Ring 1 ($P_p = -1.16$ dBm). (b) Measured coincidence counts and internal generation rate (R) and (c) CAR values as a function of the pump power.

state:

$$|\Phi\rangle = \frac{1}{\sqrt{2}}\left(|0\rangle_S|0\rangle_I + e^{i\Phi}|1\rangle_S|1\rangle_I\right). \tag{1}$$

Before measuring the entanglement, we want to assess the SFWM of each ring separately. The results are shown in Fig. 4. In general, coincidence curves from each ring resonator show a clear coincidence peak over a small background of accidentals [Fig. 4(a)]. From the coincidence rate measured at the detectors, we estimate the internal generation rate R as a function of the coupled pump power P_p. The data for both ring resonators are shown in Fig. 4(b). The curves show a clear quadratic increase with P_p until saturation due to bistability. Coincidence over accidental ratio (CAR) values are shown in Fig. 4(c). CAR values exceed 3000 at low power (an improvement of a factor of 30 with respect to the state of the art [19]) and most importantly we achieve emission rates $>10^5$ while retaining CAR>100, as expected for samples with low Raman noise.

The setup used to demonstrate entanglement is shown in Fig. 1. The idler and signal photons emitted from the sample are separated by a coarse wavelength division multiplexer (CWDM), then the frequency bins are mixed using two optical amplitude modulators ($V_\pi = 7$ V in the RF range) operated at $\Delta\nu/2$ using the same function generator. The generator can drive the two modulators at coherent but independent phases. The mixing occurs at a frequency in the middle of the two bins ($\nu_I = 190.85$ THz and $\nu_S = 195.65$ THz for idler and signal, respectively), which is then postselected using a 10 GHz tunable distributed Bragg reflector (DBR), and sent to superconducting single photon detectors (SSPDs) for coincidence counting. The total loss of the system is 21 dB or 11.5 dB per channel, of which 2 dB coming from the grating couplers, 5 dB from external filtering and multiplexing, 3.5 dB from the amplitude modulators, and 1 dB from the efficiency of the detectors.

To understand the role of the amplitude modulators in the experiment, let us first consider their effect on a general electric field $E = E_0 e^{i\omega t}$. The modulators are in the push-pull configuration, and their internal phase is modulated in time following a sinusoidal law $\Theta + \beta\sin(\Omega t + \phi)$ where Θ is a constant bias and β the modulation index. The output field E_{out} thus becomes

$$\begin{aligned} E_{out} &= \frac{E_0}{2}e^{i\omega t}\left\{e^{i\beta\sin(\Omega t+\phi)} + e^{i\Theta}e^{-i\beta\sin(\Omega t+\phi)}\right\} \\ &= \frac{E_0}{2}e^{i\omega t}\left\{\sum_{n=-\infty}^{+\infty}\left[J_{2n}(\beta)e^{i2n(\Omega t+\phi)}\left(1+e^{i\Theta}\right) + \right.\right. \\ &\left.\left. J_{2n+1}(\beta)e^{i(2n+1)(\Omega t+\phi)}\left(1-e^{i\Theta}\right)\right]\right\}, \end{aligned} \tag{2}$$

where $J_n(\beta)$ is the nth-order Bessel function and we have used the Jacobi–Anger expansion:

$$e^{i\beta\sin(\Omega t+\phi)} = \sum_{n=-\infty}^{+\infty} J_n(\beta)e^{in(\Omega t+\phi)}. \tag{3}$$

We operate the modulators with $\Theta = \pi$, so that the carrier wave is suppressed and only the odd-order terms remain in Eq. (2). Furthermore, the spectral selection operated by the Bragg filters imposes that only the first of the harmonics of Eq. (2) is actually observed, and we can simplify the expression of E_{out} by keeping only the terms in $J_1(\beta)$ and $J_{-1}(\beta) = -J_1(\beta)$:

$$\begin{aligned} E_{out} &\simeq E_0 e^{i\omega t}J_1(\beta)\left(e^{i(\Omega t+\phi)} - e^{-i(\Omega t+\phi)}\right) \\ &= 2iE_0 e^{i\omega t}J_1(\beta)\sin(\Omega t+\phi). \end{aligned} \tag{4}$$

From Eq. (4) it is easy to see the effect of the modulators on the frequency bins. For each bin, the field at the generation frequency is suppressed, while two sidebands are created at its sides with a $\pm\Omega$ shift. When working in the condition $\Omega = \Delta\nu/2$ there is perfect overlap for one sideband of each frequency bin in the middle of the two frequencies. By combining this overlap with the spectral selection performed by the Bragg filter (which selects the frequency in the middle of the frequency bins) followed by detection one performs a projective measurement on the state $|-2\phi_S\rangle = \frac{1}{\sqrt{2}}(|0\rangle - e^{-2i\phi_S}|1\rangle)$ for the signal photons and on the state $|2\phi_I\rangle = \frac{1}{\sqrt{2}}(|0\rangle - e^{2i\phi_I}|1\rangle)$ for the idler photons, being ϕ_S and ϕ_I the driving phases of the respective amplitude modulators. The part on the experimental setup following the CWDM is analogous to the polarization analyzers in experiments with polarization-encoded photons, the beam splitter and phase shifters for path-encoded photons, and the interferometers for time-bin encoded photons, respectively [12]. This approach allows one to project the state of each photon over any of the states at the equator of the respective Bloch sphere, with the projected state selected by the phases ϕ_S and ϕ_I of the two amplitude modulators.

The photon flux measured on each detector is independent of the phases of the two modulators:

$$\begin{aligned} \mathrm{Tr}\left[|\Phi\rangle\langle\Phi|\left(|-2\phi_S\rangle\langle-2\phi_S|\otimes\mathbb{1}\right)\right] &= \frac{|J_1(\beta)|^2}{2}; \\ \mathrm{Tr}\left[|\Phi\rangle\langle\Phi|\left(\mathbb{1}\otimes|2\phi_I\rangle\langle2\phi_I|\right)\right] &= \frac{|J_1(\beta)|^2}{2}. \end{aligned} \tag{5}$$

However, despite that the intensities are independent of ϕ_S and ϕ_I, the phases influence the coincidence count, which is predicted to be

$$\begin{aligned} C &= C_0\mathrm{Tr}\left[|\Phi\rangle\langle\Phi|\left(|-2\phi_S, 2\phi_I\rangle\langle-2\phi_S, 2\phi_I|\right)\right] \\ &= C_0\left|J_1(\beta)\right|^4\cos^2\left(\frac{\Phi}{2} - \phi_S + \phi_I\right), \end{aligned} \tag{6}$$

where C_0 is the coincidence count that would be generated by a single ring with the same pumping power and the same overall

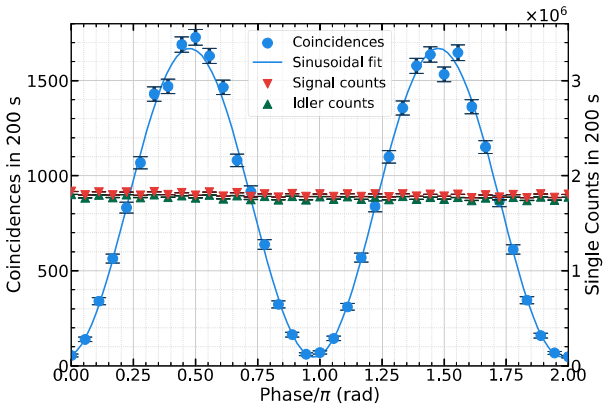

Fig. 5. Bell measurement performed at a coupled pump power $P_p \approx 2.5$ dBm. Coincidence counts (left-hand axis, blue circles) and single counts of signal (right-hand axis, red down-pointing triangle) and idler (right-hand axis, green up-pointing triangle) in 200 s.

setup losses. When measuring the coincidences as a function of the modulator phases, a visibility V exceeding $1/\sqrt{2}$ entails a violation of the CHSH inequality [17]. In actual experiments, such visibility can be limited by noise from competing processes like Raman scattering in the device or in the optical fibers connecting the device. The effect of this noise is to turn the pure, fully entangled state generated by SFWM [Eq. 1] into a mixed state with limited entanglement. Also notice that in Eqs. (5) and (6) we have only taken into account the imperfect transfer of power from the original frequency bins to the sidebands in the term $|J_1(\beta)|^2$. In actual experiments additional losses from the modulators and the filters should also be taken into account.

Our experimental results are shown in Fig. 5, where the intensities on the single detectors and the coincidence counts are plotted, with Poissonian error bars, as a function of $\phi_I - \phi_S$. As expected, single counts on both detectors are independent of the phase of the two modulators. On the contrary, coincidences show a clear interference when varying the phase difference. The interference fits well with the curve predicted by Eq. (6), with a visibility of 94.6% ± 1.1%. This proves a violation of the CHSH [17] inequalities, and thus entanglement, with a confidence interval of some 22 standard deviations.

In conclusion, we have experimentally demonstrated a silicon photonics device capable of generating frequency-bin entangled photon pairs with high rate and high CAR values. Most importantly, our results are obtained by integrating coincidence counts in the full width at half maximum (FWHM) of the coincidence peaks without any subtraction of accidental counts, therefore we are characterizing the quantum interference of the quantum state outputted from the sample, including any contribution coming from competing processes. This proves that this source is ready to be used in actual quantum information protocols. Our source has a $\Delta\nu$ of the order of 10 GHz and is realized in the silicon photonics platform; this means that our source can be directly integrated with active devices, in particular modulators, on the same chip in future iterations. Finally, our design is highly engineerable, opening the way to the realization of devices capable of generating any state on the Bloch sphere on demand. This flexibility in the design also means that more than two rings can be used, giving access to larger Hilbert spaces via the use of frequency qudits.

Funding. Ministero dell'Istruzione, dell'Università e della Ricerca (F11I18000680001).

Acknowledgments. This work has been supported by Ministero dell'Istruzione, dell'Universitá e della Ricerca [MIUR grant Dipartimenti di Eccellenza 2018-2022 (F11I18000680001)].

Disclosures. The authors declare no conflicts of interest.

Data availability. The data that support the findings of this study are available from the corresponding author upon reasonable request.

REFERENCES

1. L. Caspani, C. Xiong, B. J. Eggleton, D. Bajoni, M. Liscidini, M. Galli, R. Morandotti, and D. J. Moss, Light: Sci. Appl. **6**, e17100 (2017).
2. P. G. Kwiat, E. Waks, A. G. White, I. Appelbaum, and P. H. Eberhard, Phys. Rev. A **60**, R773 (1999).
3. J. W. Silverstone, R. Santagati, D. Bonneau, M. J. Strain, M. Sorel, J. L. O'Brien, and M. G. Thompson, Nat. Commun. **6**, 7948 (2015).
4. J. Brendel, N. Gisin, W. Tittel, and H. Zbinden, Phys. Rev. Lett. **82**, 2594 (1999).
5. J. D. Franson, Phys. Rev. Lett. **62**, 2205 (1989).
6. L. Olislager, J. Cussey, A. T. Nguyen, P. Emplit, S. Massar, J.-M. Merolla, and K. P. Huy, Phys. Rev. A **82**, 013804 (2010).
7. F. Kaneda, H. Suzuki, R. Shimizu, and K. Edamatsu, Opt. Express **27**, 1416 (2019).
8. D. Rieländer, A. Lenhard, O. J. Farìas, A. Máttar, D. Cavalcanti, M. Mazzera, A. Acín, and H. de Riedmatten, Quantum Sci. Technol. **3**, 014007 (2018).
9. C. L. Morrison, F. Graffitti, P. Barrow, A. Pickston, J. Ho, and A. Fedrizzi, APL Photonics **7**, 066102 (2022).
10. M. Kues, C. Reimer, P. Roztocki, L. R. Cortés, S. Sciara, B. Wetzel, Y. Zhang, A. Cino, S. T. Chu, B. E. Little, D. J. Moss, L. Caspani, J. Aza na, and R. Morandotti, Nature **546**, 622 (2017).
11. S. Clemmen, A. Farsi, S. Ramelow, and A. L. Gaeta, Phys. Rev. Lett. **117**, 223601 (2016).
12. P. Imany, J. A. Jaramillo-Villegas, O. D. Odele, K. Han, D. E. Leaird, J. M. Lukens, P. Lougovski, M. Qi, and A. M. Weiner, Opt. Express **26**, 1825 (2018).
13. C. Reimer, M. Kues, P. Roztocki, B. Wetzel, F. Grazioso, B. E. Little, S. T. Chu, T. Johnston, Y. Bromberg, L. Caspani, D. J. Moss, and R. Morandotti, Science **351**, 1176 (2016).
14. L. G. Helt, M. Liscidini, and J. E. Sipe, J. Opt. Soc. Am. B **29**, 2199 (2012).
15. N. Wada, S. Solin, J. Wong, and S. Prochazka, J. Non-Cryst. Solids **43**, 7 (1981).
16. M. Liscidini and J. E. Sipe, Opt. Lett. **44**, 2625 (2019).
17. J. F. Clauser, M. A. Horne, A. Shimony, and R. A. Holt, Phys. Rev. Lett. **23**, 880 (1969).
18. F. Boeuf, A. Fincato, L. Maggi, J. F. Carpentier, P. L. Maitre, M. Shaw, S. Cremer, N. Vulliet, C. Baudot, S. Monfray, S. Jan, C. Deglise, J. R. Manouvrier, C. Durand, A. Simbula, D. Goguet, P. Bar, D. Ristoiu, F. Leverd, L. Babaud, A. Daverio, M. Binda, A. Bazzotti, A. Cancamilla, L. Ramini, M. Traldi, and P. Gambini, '*2019 IEEE International Electron Devices Meeting (IEDM)*,' (2019).
19. H.-H. Lu, K. V. Myilswamy, R. S. Bennink, S. Seshadri, M. S. Alshaykh, J. Liu, T. J. Kippenberg, D. E. Leaird, A. M. Weiner, and J. M. Lukens, Nat. Commun. **13**, 4338 (2022).